Dihydrogen phosphate ion functionalized nanocrystalline thallium ruthenium oxide pyrochlore as a bifunctional electrocatalyst for aqueous Na-air batteries

Myeongjin Kim, Hyun Ju, Jooheon Kim*

School of Chemical Engineering & Materials Science, Chung-Ang University, 211 Heukseok-dong, Dongjak-gu, Seoul, 156-756, Republic of Korea

ABSTRACT

The sodium-air (Na–air) batteries are considered as a new promising energy storage devices due to their 1683 W h kg^{-1} of high theoretical specific energy density. However, these outstanding theoretical energy density performances cannot be achieved because undesirable sluggish oxygen evolution reaction (OER) and oxygen reduction reaction (ORR) reaction kinetics on the air cathode side causes the high overpotential gap and low round-trip efficiencies during charge-discharge process. Therefore, the development of highly active bifunctional oxygen electrocatalysts is the key strategy to obtain the low overpotential gap with high energy density performance of Na-air batteries. In this work, a novel single crystalline thallium ruthenium oxide ($Tl_2Ru_2O_7$) with pyrochlore structure was firstly revealed as an effective bifunctional electrocatalyst. Moreover, in order to enhance the surface chemical reactivity of $Tl_2Ru_2O_7$, the surface of $Tl_2Ru_2O_7$ is functionalized by using the dihydrogen phosphate ion ($P-Tl_2Ru_2O_7$) for achieving the effective and rapid charge transfer behavior. The superior bifunctional catalytic activity of $P-Tl_2Ru_2O_7$ can be explained by the degree of covalency of Ru-O bonds in $Tl_2Ru_2O_7$ and enhanced covalent character by functionalized dihydrogen phosphate ion, which can afford favorable oxidation nature to Tl and Ru ions.

1. Introduction

Recently, serious issues regarding the energy demands have resulted in the extensive development and research of new energy conversion and storage solutions [1]. Among the diverse electrical energy storage system (EES), the metal-air batteries which exhibit extremely high energy density performance have lots of potential for effective energy storage device [2–7]. Especially, the 1683 W h kg^{-1} of high theoretical specific energy density performance of sodium-air (Na–air) batteries are focused on as attractive candidate among the various metal-air batteries [8,9]. Unfortunately, considerable researches cannot reach to the theoretical specific energy density performance of Na–air batteries because of the high overpotential gap and low round-trip efficiencies during charge-discharge process [10]. The ideal Na–air batteries must show the plateau regions for charge-discharge curves at around theoretical cell voltage. However, the voltage of these plateau regions is deviated from the theoretical cell voltage due to the undesirable oxygen evolution reaction (OER) and oxygen reduction reaction (ORR) bifunctional catalytic activities on the air electrode [11]. Especially, the deviated plateau regions for discharge curves are shown at the lower voltage

than the theoretical cell voltage, resulting in the decrease of integrated area of discharge profile. This phenomenon leads to the decrease of energy density performance of Na–air batteries and provide the reason for the difficulties to achieve the theoretical energy density performance of Na–air batteries [12]. Therefore, although extensive efforts have been devoted to reduce the overpotential gap between charge and discharge plateau by developing the OER and ORR bifunctional electrocatalyst, the reported round-trip efficiencies are still not enough to achieve the theoretical energy density performance [13–16].

To date, the various bifunctional ORR and OER electrocatalysts such as metal oxide materials, nonprecious metals, metal free-based materials are reported [17–25]. Among these, pyrochlore oxides ($A_2B_2O_7$), which are a family of complex oxides, have been considerably studied to obtain the high ORR and OER bifunctional catalytic activities. Generally, the ruthenium (Ru) 4-d transition metal is considered as ideal B-site cation for highly active electrocatalytic pyrochlore oxides because the high spin energy state of 4d eg orbital of Ru can easily hybrid the Ru 4d and oxygen 2p orbitals, enabling the metallic conduction properties of pyrochlore oxides [26]. These metallic conduction pyrochlore oxides exhibit high electrical conductivity with high charge transfer and
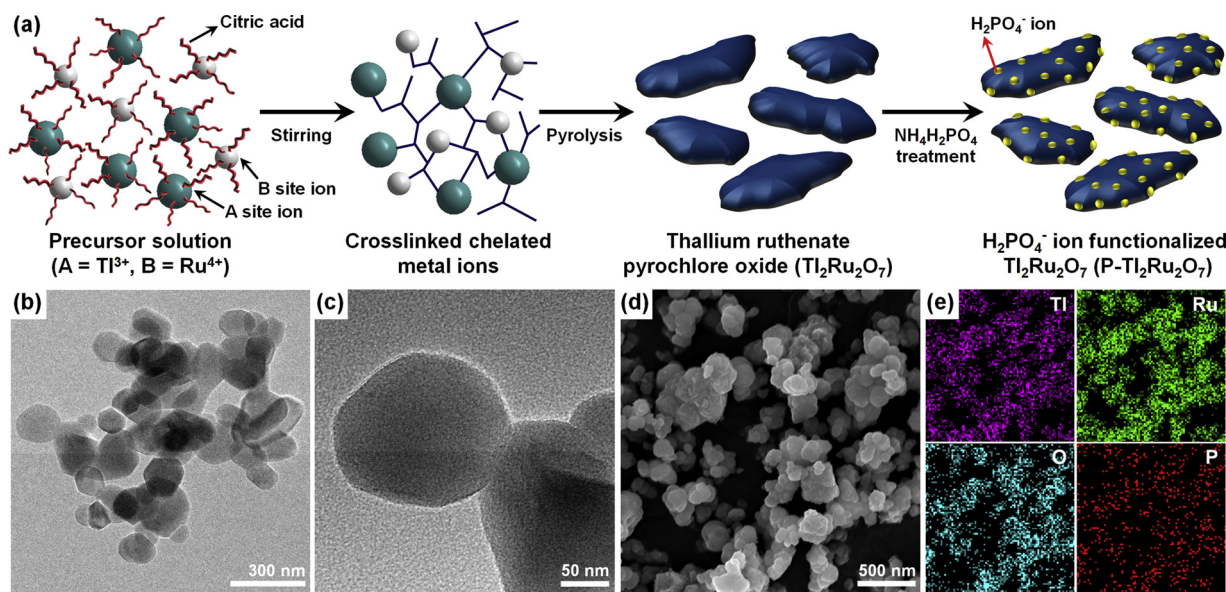
Fig. 1. (a) Schematic representation of the preparation of P-Tl$_2$Ru$_2$O$_7$. (b) Low magnification of HR-TEM image for P-Tl$_2$Ru$_2$O$_7$. (c) High magnification of HR-TEM image for P-Tl$_2$Ru$_2$O$_7$. (d) FE-SEM image of P-Tl$_2$Ru$_2$O$_7$. (e) EDX elements mapping image for P-Tl$_2$Ru$_2$O$_7$.

excellent catalytic activities [26]. Therefore, the various Ru-based pyrochlore oxides, such as Bi$_{2.4}$Ru$_{1.6}$O$_7$, Pb$_2$Ru$_2$O$_{6.5}$, Bi$_2$[Ru$_{2-x}$Bi$_x$]O$_{7-y}$, Bi$_2$Ru$_2$O$_7$, Pb$_2$[Ru$_{2-x}$Pb$_x^{4+}$]O$_{6.5}$ and Pb$_2$Ru$_2$O$_{7-x}$, are developed for bifunctional electrocatalyst [27–33]. For the A-site selection, the adopted A-site cations must exhibit the small differences of Pauling electronegativities with Ru. The small differences of electronegativities between B-site Ru cation and A-site cation are beneficial to create the high density of covalent chemical bond between Ru-O-Ru/A-site cation. Therefore, the large covalent bond can facilitate to delocalize the outermost orbitals of metal cations, creating the shared electrons. These shared electrons can promote the fast charge transfer during electrocatalysis [26]. However, the most previous researches were focused on the use of Bi^{3+} and Pb^{2+} cations as A-site cations for pyrochlore oxides, limiting the development of additional A-site cations. Considering the similar electronegativities with Ru and ionic radius with Bi^{3+} and Pb^{2+} cations, the Tl^{3+} cation can be regarded as a new candidate for A-site cation of Ru-based pyrochlores. Therefore, outstanding catalytic activities of Tl$_2$Ru$_2$O$_7$ can be achieved by the metallic conduction behavior due to the strong hybridization between Ru 4d and O 2p orbitals and efficient charge transfer caused by 0.16 of small differences of Tl (2.04) and Ru (2.2) electronegativities.

Herein, we report the first use of Tl$_2$Ru$_2$O$_7$ pyrochlore oxide nanoparticles as efficient OER and ORR electrocatalysts for Na-air batteries, which have never been studied as bifunctional electrocatalyst. Moreover, to boost the electrocatalytic activity, the surface of Tl$_2$Ru$_2$O$_7$ was functionalized by dihydrogen phosphate (H$_2$PO$_4^-$) ion (P-Tl$_2$Ru$_2$O$_7$). In a recent work, Jo et al. reported the highly improved photo-electrochemical water oxidation activity by phosphate doping into BiVO$_4$ photoanode due to the rapid charge-transfer [34]. Also, Zhai et al. functionalized the phosphate ion on the surface of Co$_3$O$_4$ nanosheet to enhance the surface reactivity by improvement of charge transfer behavior for vigorous redox-reaction, which causes the enhanced pseudo-capacitive performance [35]. Using these results, the surface reactivity of Tl$_2$Ru$_2$O$_7$ can be tuned by H$_2$PO$_4^-$ ion functionalization. The enhanced surface chemical reactivity of Tl$_2$Ru$_2$O$_7$ is caused by the smaller electronegativity of H$_2$PO$_4^-$ ion than oxygen. The low electronegativity of H$_2$PO$_4^-$ ion can enable not only the fast charge transfer by the improvement of covalent character of Tl-OPO(OH)$_2$ and Ru-OPO(OH)$_2$ bond but also the favorable oxidation nature of Tl and Ru cations by the weak attraction to electrons between -OPO(OH)$_2$ and 6p and 4d orbitals of Tl and Ru cations. Therefore, the facile

extraction of electrons by low energy can deliver high OER and ORR catalytic activities by promoting the oxidation nature of Tl and Ru cations, which can easily donate the electrons to electrolyte and transfer to inner layer of Tl$_2$Ru$_2$O$_7$. Finally, based on these improved bifunctional catalytic activities, the P-Tl$_2$Ru$_2$O$_7$ air-cathode shows high round-trip efficiency for half cell Na-air battery with decreased voltage gap between average charge-discharge voltages for full cell Na-air battery.

2. Experimental

2.1. Synthesis of dihydrogen phosphate ion functionalized thallium ruthenium pyrochlore (P-Tl$_2$Ru$_2$O$_7$)

Tl$_2$Ru$_2$O$_7$ was synthesized by sol-gel method from uniformly cross-linked Tl^{3+} and Ru^{4+} ions with citric acid (C$_6$H$_8$O$_7$) as a chelating agent. The buffer solution was obtained by the fabrication of a mixture of 1.5 mL nitric acid, 3.42×10^{-2} mol anhydrous ethylenediaminetetraacetic acid and 1 M ammonia solution until the pH of the solution reached 7. To synthesize the Tl$_2$Ru$_2$O$_7$, the Ru^{4+} precursor (0.2614 g of ruthenium (III) nitrosyl nitrate solution), the Tl^{3+} precursor (0.3136 g of thallium (III) acetate) and 10 g anhydrous C$_6$H$_8$O$_7$ were dissolved and stirred with the 500 mL of buffer solution during 24 h at 150 °C until the gelled solution mixture obtained. Then, the gelled solution was dried in an oven at 200 °C for 12 h. The obtained powders were calcined and crystallized at 1200 °C for 8 h in air atmosphere to produce single crystalline Tl$_2$Ru$_2$O$_7$ nanoparticles. In order to functionalize the dihydrogen phosphate ion, the Tl$_2$Ru$_2$O$_7$ nanoparticles (0.5 g) were suspended in a 0.5 M ammonium dihydrogen phosphate solution (100 mL) at 120 °C in a water-cooled condenser with vigorous stirring for 36 h. After the treatment, the resulting particles were rinsed with deionized water (DI-water), filtered three times and vacuum-dried at 80 °C for 12 h.

2.2. Characterization methods

To obtain the catalyst electrode, the synthesized Tl$_2$Ru$_2$O$_7$ and P-Tl$_2$Ru$_2$O$_7$ catalyst (7.5 mg) was mixed with 5 wt% Nafion (0.038 mL, 5 wt% in isopropanol), ethanol (0.86 mL) and DI-water (0.1 mL). The resulting slurry was ultra-sonicated for 30 min to generate a catalyst ink. The 10.0 μL of catalyst ink was pipetted onto the 0.25 cm^2 glassy carbon electrode. The loading level of P-Tl$_2$Ru$_2$O$_7$ and Tl$_2$Ru$_2$O$_7$ on the
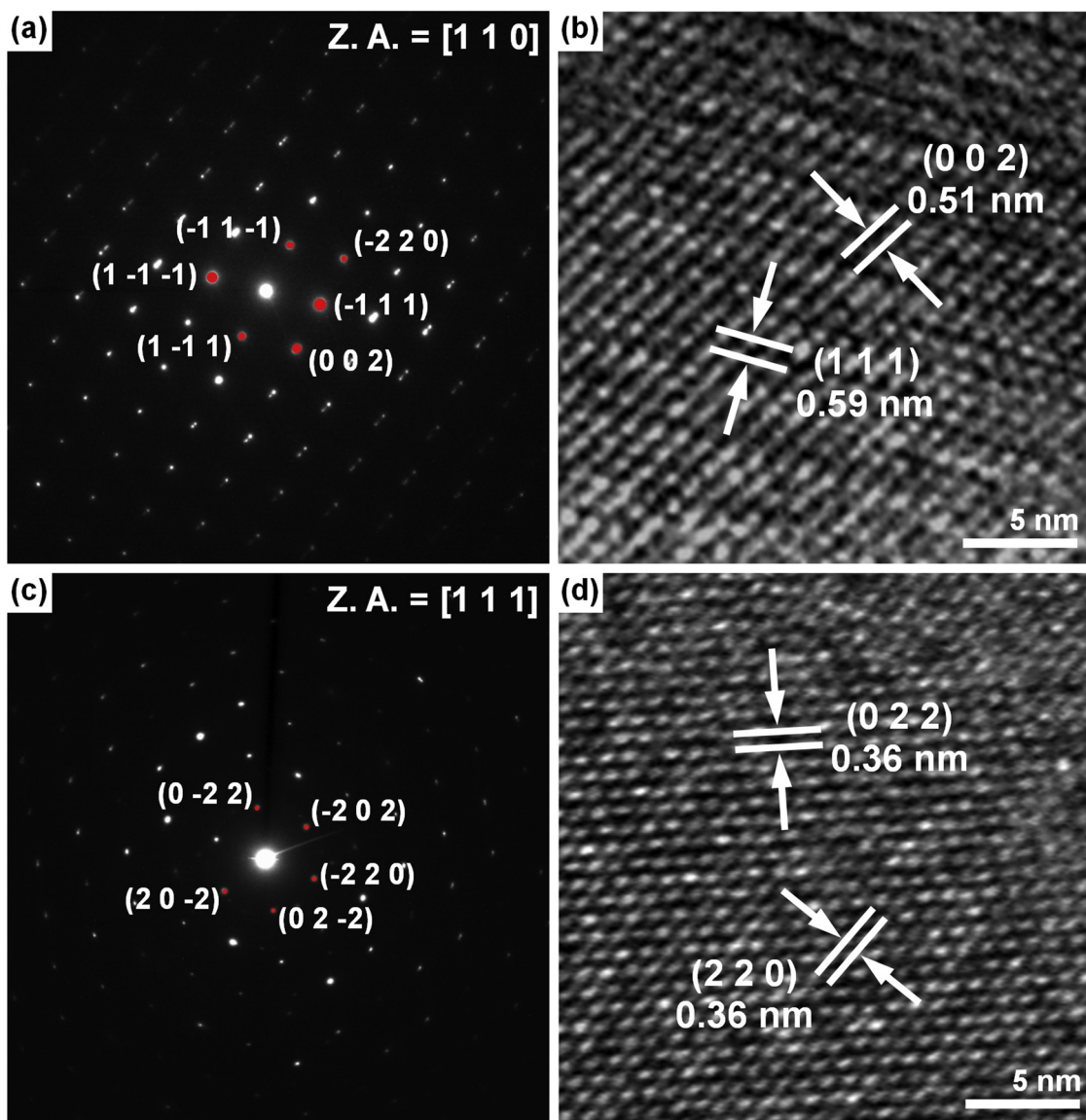
Fig. 2. (a) SAED patterns for P-Tl$_2$Ru$_2$O$_7$ along the [1 1 0] zone axis. (b) High-magnification HR-TEM image of P-Tl$_2$Ru$_2$O$_7$. (c) SAED patterns for P-Tl$_2$Ru$_2$O$_7$ along the [1 1 1] zone axis. (d) High-magnification HR-TEM image of P-Tl$_2$Ru$_2$O$_7$.

glassy carbon electrode is 0.5701 mg$_{cat}$ cm^{-2} and 0.5712 mg$_{cat}$ cm^{-2}, respectively. 20 wt% Pt on Vulcan carbon black (Pt/C, FuelCellStore) and 20 wt% Ir on Vulcan (Ir/C, FuelCellStore) were measured for comparison. The Pt/C and Ir/C catalyst ink was obtained by making the mixture of the Pt/C (or Ir/C) catalyst (5 mg) with 5 wt% Nafion (0.04 mL, in isopropanol), ethanol (1.06 mL) and DI-water (0.1 mL), then ultrasonicated for 30 min. The 6.0 μL of catalyst ink was pipetted onto the 0.25 cm^2 glassy carbon electrode. The loading level of 20 wt% Pt/C and 20 wt% Ir/C is 0.259 mg$_{(20\% \ Pt/C)}$ cm^{-2} and 0.278 mg$_{(20\% \ Ir/C)}$ cm^{-2}, resulting in the 51.8 μg$_{Pt}$ cm^{-2} of pure Pt and 55.6 μg$_{Ir}$ cm^{-2} of pure Ir, respectively. The rotating disk electrode (RDE) technique was employed to measure the ORR and OER catalytic activities for Tl$_2$Ru$_2$O$_7$, P-Tl$_2$Ru$_2$O$_7$, Pt/C and Ir/C catalyst by three-electrode cell setup which is consisted of glassy carbon rotating disk electrode, Ag/AgCl and a Pt wire as a working, reference and counter electrode in 0.1 M KOH aqueous electrolyte. Before conducting RDE experiment, the 0.1 M KOH aqueous electrolyte was saturated with oxygen by purging the pure oxygen gas (99.9%) for 30 min. All of the OER and ORR catalytic activities are converted to versus the reversible hydrogen electrode (RHE), and the obtained potentials (vs Ag/AgCl) were converted to RHE by using following Eq. (1):

$$E_{RHE} = E_{Ag/AgCl} + 0.0592 \, pH + E_{Ag/AgCl}° \tag{1}$$

Where, pH = 12.9 for 0.1 M KOH and $E_{Ag/AgCl}°$ (in 1 M KCl) = +0.235 V. Koutecky-Levich (K–L) plots were obtained at various potentials. The slope of their best linear fit lines was used to calculate the number electrons transferred (n) on the basis of the following Equation (2):

$$\frac{1}{J} = \frac{1}{J_L} + \frac{1}{J_K} = \frac{1}{B\omega^{1/2}} + \frac{1}{J_K} \tag{2}$$

where, ω, B, J_K, J_L and J are the electrode rotation speed, B-factor, kinetic limiting current density, diffusion limiting current density and measured disk current density, respectively. Moreover, the B-factor can be obtained by the following Eq. (3):

$$B = 0.62nFC_oD_o^{2/3}\nu^{-1/6} \tag{3}$$

where, ν, C_o, D_o, F and n are the 0.01 cm^2 s^{-1} of kinetic viscosity of the solution, 1.2×10^{-6} mol cm^{-3} of concentration of O$_2$ dissolved in 0.1 M KOH, 1.9×10^{-5} cm^2 s^{-1} of diffusion coefficient of O$_2$ in 0.1 M KOH, 96,485 C mol^{-1} of Faraday constant and apparent number of electrons transferred in the reaction, respectively. When the rotation speed is
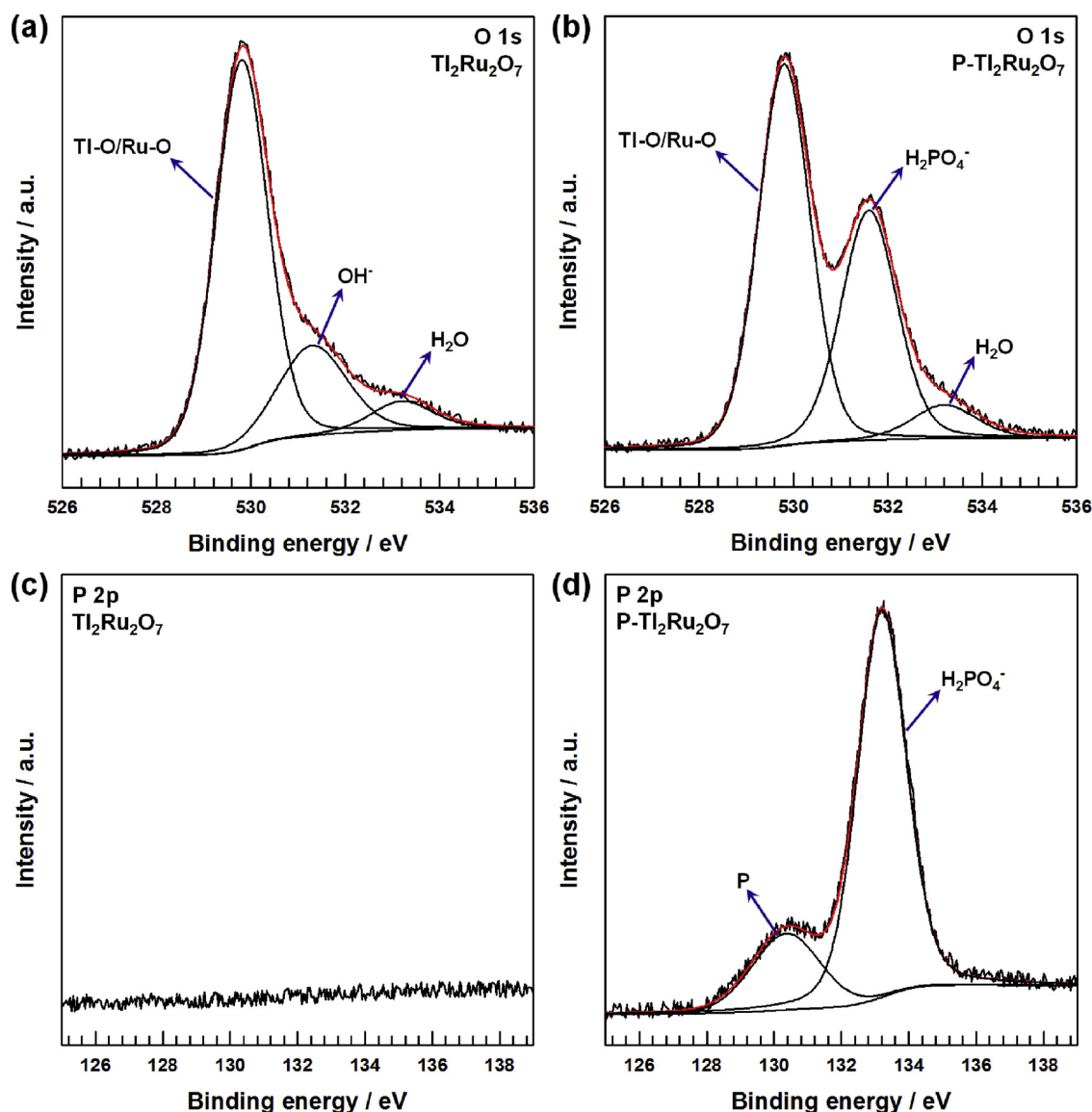
Fig. 3. (a) XPS O 1 s spectra of $Tl_2Ru_2O_7$. (b) XPS O 1 s spectra of P-$Tl_2Ru_2O_7$. (c) XPS P 2p spectra of $Tl_2Ru_2O_7$. (d) XPS P 2p spectra of P-$Tl_2Ru_2O_7$.

expressed in rad, the constant 0.62 is adopted. The Tafel slope was obtained from the Linear sweep voltammetry (LSV) curves by applying the following Tafel Eq. (4):

$$\eta = a + b \cdot \log |J| \tag{4}$$

where, b, J and η are the Tafel slope, current density and overpotential, respectively. For the rotating ring-disk electrode (RRDE) measurements, catalyst inks and electrodes were prepared by the same as for RDE. The RRDE voltammograms were conducted consisting of a Pt ring electrode and a glassy carbon disk electrode. To analyze the OER mechanism and reaction pathway, the detection of peroxide intermediates was conducted by fixing the Pt ring potential at 1.5 V vs RHE with a scan rate of 10 mV s^{-1} and rotation rate of 1600 rpm in O_2-saturated 0.1 M KOH solution.

The electrochemically active surface areas (ECSAs) of 20% Pt/C and 20% Ir/C were determined by H desorption in the CV curve based on a specific charge density of 210 μC cm_{Pt}^{-2}, 218 μC cm_{Ir}^{-2}, using the following Eq. (5):

$$ECSA = \frac{Q_H}{C \times m \times v} \tag{5}$$

Where, Q_H is the hydrogen desorption charge in the CV curve and C is

the specific charge density of Pt and Ir, and m is the weight of the Pt and Ir in the 20% Pt/C and 20% Ir/C, and v is the scan rate of CV curve.

2.3. Preparation and characterization of Na-air battery

The catalyst adopted air cathode was prepared as follows: the 10 wt % of polyvinylidene fluoride as a binder, 90 wt% of catalysts as active catalytic materials are dispersed in *N*-methyl-2-pyrrolidone as a solvent to fabricate the catalyst slurry. Then, the resulting catalyst slurry was sprayed onto one side of the carbon paper (the area of the carbon paper : 4 cm^2, FuelCellStore). The loading mass of the catalyst was 2.5 mg cm^{-2}. The metallic sodium electrode (negative electrode) was attached on nickel mesh and inserted into the pouch cell in a glove box, and an organic electrolyte (1 M NaCF$_3$SO$_3$/TEGDME) was injected. Thereafter, the solid electrolyte membrane (NASICON) was separated the air cathode and metallic sodium anode with one side in contact with the organic electrolyte and the other side of the NASICON exposed to air and the pouch cell was sealed. The round-trip efficiency for fabricated hybrid Na-air batteries was calculated by following Eq. (6):

$$Round\ trip\ efficiency\ (\%) = \frac{Average\ discharge\ voltage}{Average\ charge\ voltage} \times 100 \tag{6}$$
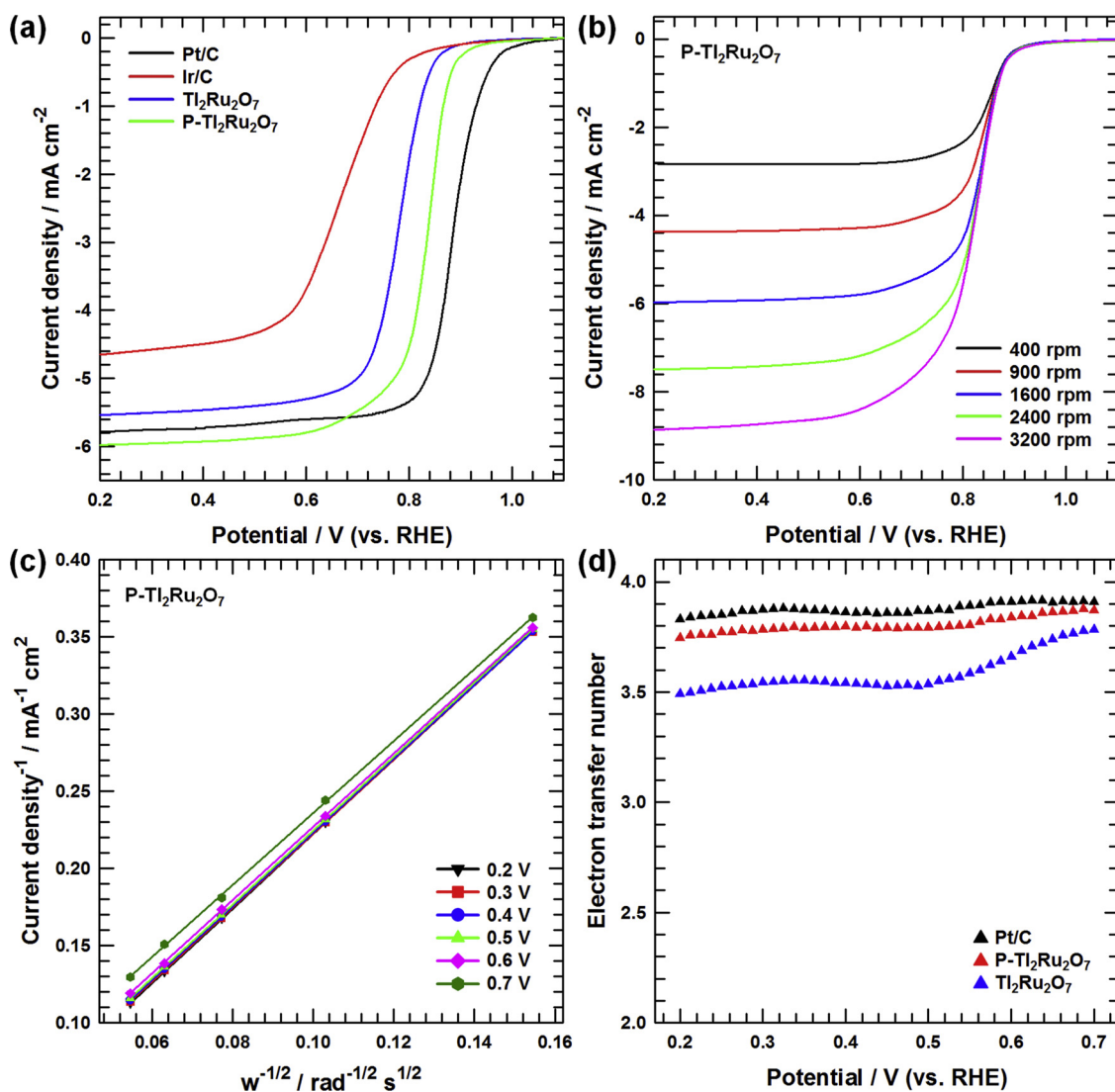
Fig. 4. (a) ORR polarization curves for P-$Tl_2Ru_2O_7$, $Tl_2Ru_2O_7$, Pt/C and Ir/C in O_2-saturated 0.1 M KOH (Rotation rate : 1600 rpm, Scan rate : 10 mV s^{-1}). (b) ORR polarization curves for P-$Tl_2Ru_2O_7$ at different rotating speed with a scan rate of 10 mV s^{-1}. (c) Koutecky-Levich plots derived from the ORR LSV curves of P-$Tl_2Ru_2O_7$. (d) Electron transfer number for P-$Tl_2Ru_2O_7$, $Tl_2Ru_2O_7$ and Pt/C at different potentials.

The power density (P_s) of Na-air batteries was calculated by following Eq. (7):

$$P_s = I_s \times V_{ad} \qquad (7)$$

where V_{ad} and I_s are the average discharge voltage and applied current density, respectively. Moreover, the further detailed characterization methods were summarized in supporting information.

3. Results and discussion

3.1. Preparation and characterization of P-$Tl_2Ru_2O_7$ catalysts

Fig. 1(a) shows the preparation route for the dihydrogen phosphate ion functionalized $Tl_2Ru_2O_7$ pyrochlore oxide. The uniformly cross-linked Ru^{4+} and Tl^{3+} cations were calcined at 1200 °C to produce the single crystalline $Tl_2Ru_2O_7$ nanoparticles. Finally, the dihydrogen phosphate ($H_2PO_4^-$) ions were functionalized on the surface of $Tl_2Ru_2O_7$ nanoparticles by ammonium dihydrogen phosphate ($NH_4H_2PO_4$) treatment. To observe the morphology, Fig. 1(b and c) and (d) show the high-resolution transmission electron microscopy (HR-TEM) and field-emission scanning electron microscopy (FE-SEM) images of P-$Tl_2Ru_2O_7$. The aggregated P-$Tl_2Ru_2O_7$ nanoparticles show

the smaller particle size than 200 nm, with irregular polyhedral morphologies. The Energy-dispersive X-ray spectrometry (EDX) elemental mapping results for P-$Tl_2Ru_2O_7$ represent the detection of uniformly distributed each element (Tl, Ru, O, and P) on the P-$Tl_2Ru_2O_7$ nanoparticles, indicating complete dihydrogen phosphate ion functionalization on the surface (Fig. 1(e)). Moreover, the atomic ratio of Tl to Ru for $Tl_2Ru_2O_7$ and P-$Tl_2Ru_2O_7$ shows *ca.* 1, confirming that the both samples belong to the pyrochlore oxide structure and these structures are well maintained during $H_2PO_4^-$ ion functionalization (Figure S1). X-ray diffraction (XRD) pattern of $Tl_2Ru_2O_7$ was clearly revealed the Fd-3 m of space group with the cubic phase crystal structure (Figure S2). Moreover, the XRD pattern for P-$Tl_2Ru_2O_7$ also shows the cubic phase structure, representing that there is no phase change during $H_2PO_4^-$ ion functionalization, which shows a good agreement with EDX spectra.

The cubic structure of the pyrochlore oxide is further confirmed by the selected–area electron diffraction (SAED) pattern, showing the unit spots of (-1 1 1) and (-1 1 -1) along with the [1 1 0] main zone axis (Fig. 2(a)). Moreover, the diffraction planes for (1 1 1) and (0 0 2) are clearly observed with the 0.59 and 0.51 nm of lattice interlayer distance, respectively (Fig. 2(b)). In the same manner, the unit spots of (-2 0 2) and (0–2 2) along with the [1 1 1] main zone axis also verify the
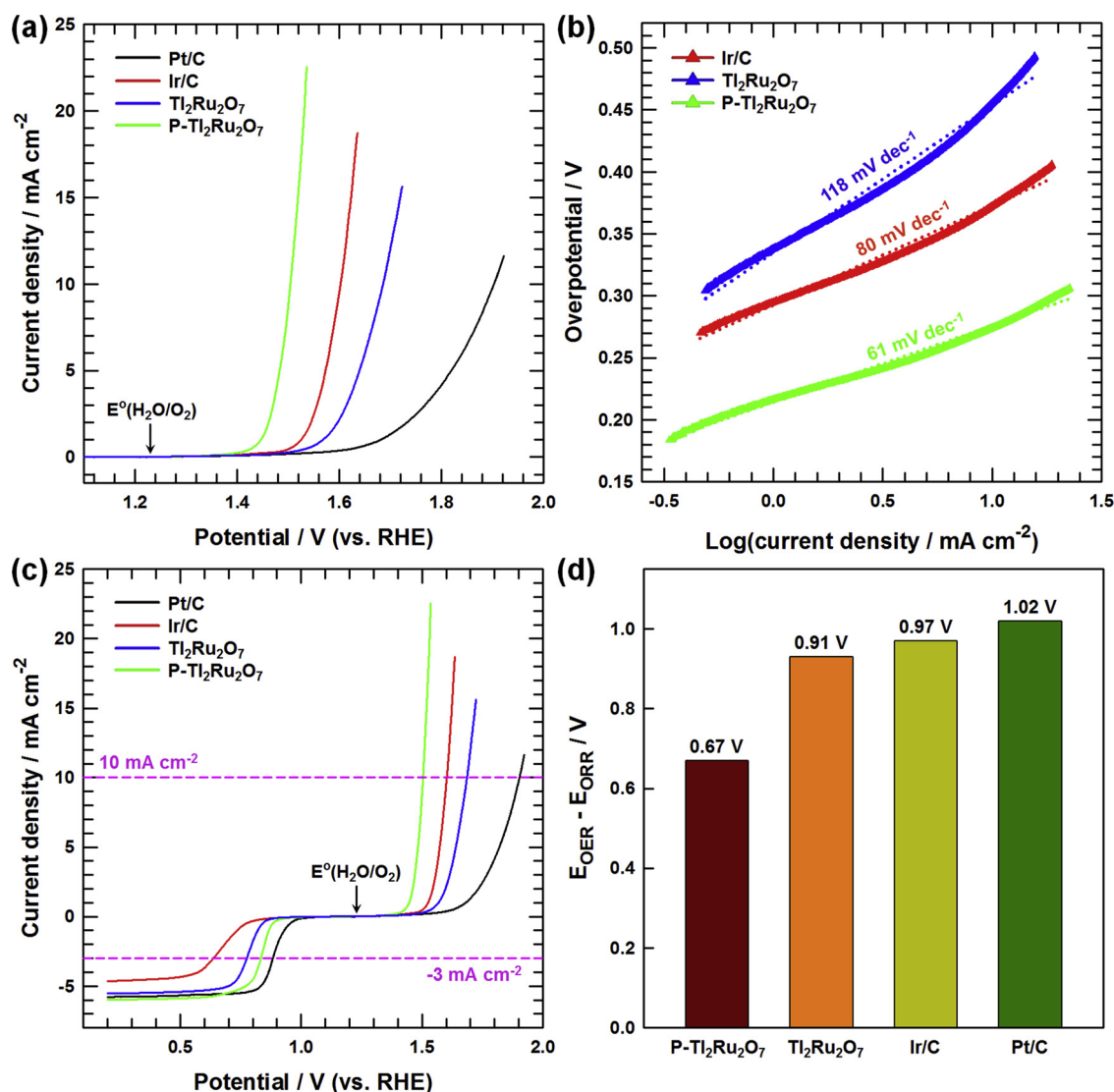
Fig. 5. (a) OER polarization curves for P-Tl$_2$Ru$_2$O$_7$, Tl$_2$Ru$_2$O$_7$, Pt/C and Ir/C in O$_2$-saturated 0.1 M KOH (Rotation rate : 1600 rpm, Scan rate : 10 mV s^{-1}). (b) Tafel plots for P-Tl$_2$Ru$_2$O$_7$, Tl$_2$Ru$_2$O$_7$ and Ir/C. (c) The overall polarization curves for P-Tl$_2$Ru$_2$O$_7$, Tl$_2$Ru$_2$O$_7$, Pt/C and Ir/C catalysts within the ORR and OER potential window. (d) Comparison of oxygen electrode activity of P-Tl$_2$Ru$_2$O$_7$, Tl$_2$Ru$_2$O$_7$, Pt/C and Ir/C.

typical cubic phases, with the 0.36 nm of lattice d-spacing for the both (2 2 0) and (0 2 2) diffraction planes (Fig. 2(c) and (d)). Furthermore, the surface functionalization of Tl$_2$Ru$_2$O$_7$ was investigated by X-ray photoelectron spectroscopy (XPS). The O 1 s core-level XPS spectra of both Tl$_2$Ru$_2$O$_7$ and P-Tl$_2$Ru$_2$O$_7$ samples display the metal-oxygen bonding peak (Tl-O/Ru-O) at 529.8 eV and physically or chemically bonded water within the Tl$_2$Ru$_2$O$_7$ and P-Tl$_2$Ru$_2$O$_7$ surface at 533.2 eV. The shoulder peak observed at 531.3 eV for the Tl$_2$Ru$_2$O$_7$ is originated from the −OH (hydroxyl groups) on the Tl$_2$Ru$_2$O$_7$ surface. Interestingly, the shoulder peak (531.6 eV) of P-Tl$_2$Ru$_2$O$_7$ is associated with the oxygen species of the H$_2$PO$_4^-$ ion (Fig. 3(a) and (b)) [35]. These shoulder peaks clearly demonstrate that the hydroxyl groups on the Tl$_2$Ru$_2$O$_7$ surface have been substituted by the H$_2$PO$_4^-$ ions on P-Tl$_2$Ru$_2$O$_7$ during NH$_4$H$_2$PO$_4$ treatment. The more deep evidence for the functionalization of H$_2$PO$_4^-$ ion on Tl$_2$Ru$_2$O$_7$ were confirmed in the deconvoluted XPS P 2p spectrum (Fig. 3(c) and (d)).

3.2. Bifunctional ORR and OER electrocatalytic activity of P-Tl$_2$Ru$_2$O$_7$ catalysts

The ORR and OER catalytic activities for as-synthesized Tl$_2$Ru$_2$O$_7$

and P-Tl$_2$Ru$_2$O$_7$ catalyst were examined in an O$_2$-saturated 0.1 M KOH aqueous electrolyte by RDE technique. In order to benchmark the ORR and OER performance, the commercial Pt/C and Ir/C catalysts were also measured. Figure S3 represents the cyclic voltammetry (CV) curves for P-Tl$_2$Ru$_2$O$_7$ and Tl$_2$Ru$_2$O$_7$ catalysts in an O$_2$- and N$_2$-saturated KOH solution. In O$_2$-saturated electrolyte, there are obvious ORR cathodic reduction peaks, showing the higher reduction onset potential for P-Tl$_2$Ru$_2$O$_7$ catalyst ($\sim$0.9 V vs RHE) than Tl$_2$Ru$_2$O$_7$ ($\sim$0.85 V vs RHE). This result indicates the better ORR activity of P-Tl$_2$Ru$_2$O$_7$ catalyst. The ORR LSV curve of P-Tl$_2$Ru$_2$O$_7$ catalyst implies that the ORR activity of P-Tl$_2$Ru$_2$O$_7$ is much improved compared to Tl$_2$Ru$_2$O$_7$ due to the dihydrogen phosphate ion functionalization, confirmed by the limiting current density and onset potential (P-Tl$_2$Ru$_2$O$_7$: -5.975 mA cm^{-2} and $\sim$0.89 V, Tl$_2$Ru$_2$O$_7$: -5.537 mA cm^{-2} and $\sim$0.83 V) (Fig. 4(a)). Moreover, the higher ORR activity of P-Tl$_2$Ru$_2$O$_7$ than Tl$_2$Ru$_2$O$_7$ was also observed by confirming the reduction potential at −3 mA cm^{-2} of current density (P-Tl$_2$Ru$_2$O$_7$: 0.834 V, Tl$_2$Ru$_2$O$_7$: 0.774 V). Although the P-Tl$_2$Ru$_2$O$_7$ exhibits a slightly lower ORR reduction and onset potential than those of Pt/C, the P-Tl$_2$Ru$_2$O$_7$ shows the comparable and even more outstanding ORR catalytic activities compared with previously reported electrocatalysts (Table S1). To normalize the catalytic
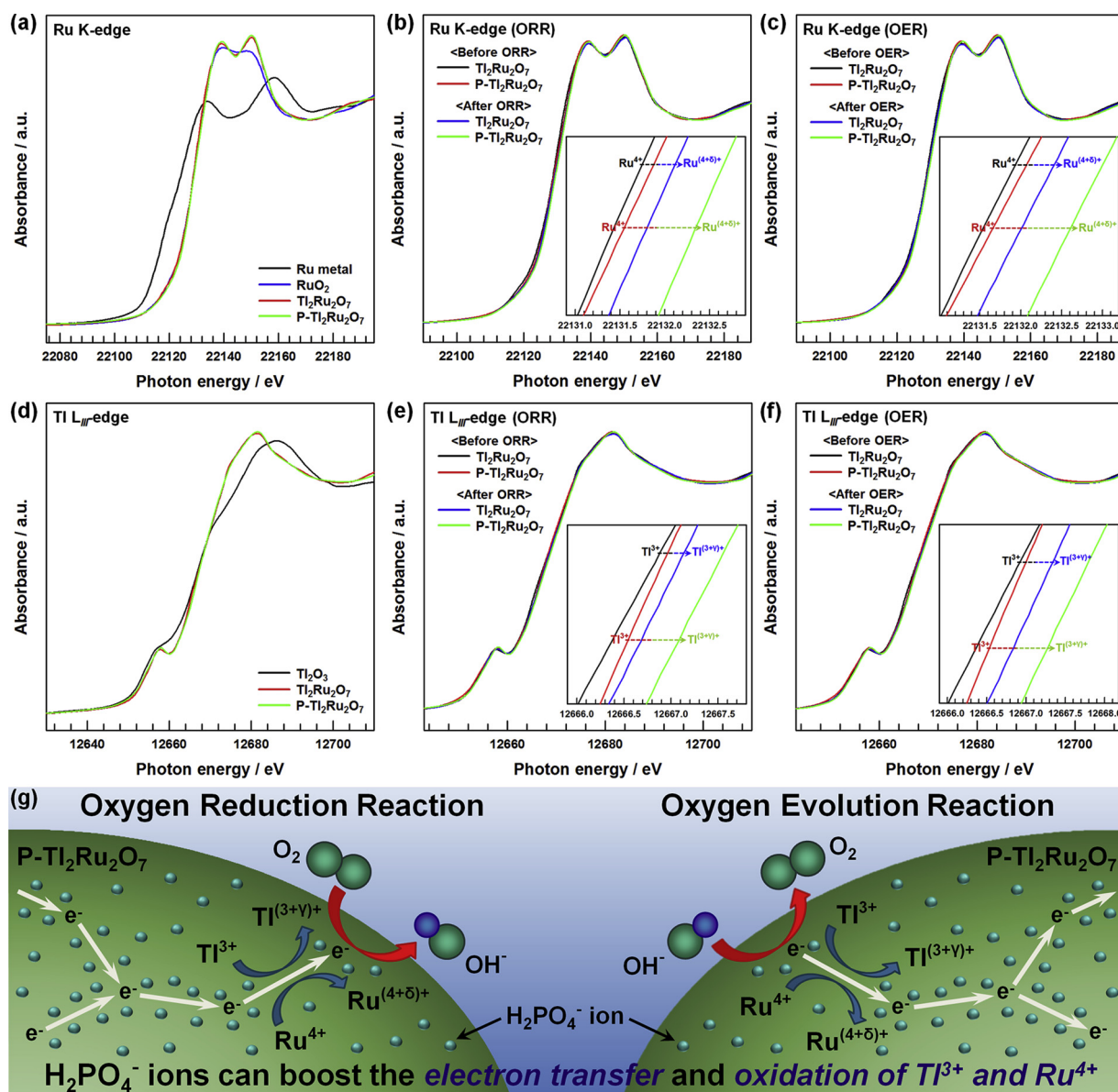
Fig. 6. Normalized Ru K-edge XANES spectra of (a) Ru metal, RuO₂, P-Tl₂Ru₂O₇ and Tl₂Ru₂O₇. (b) P-Tl₂Ru₂O₇ and Tl₂Ru₂O₇ before and after ORR. (c) P-Tl₂Ru₂O₇ and Tl₂Ru₂O₇ before and after OER. Normalized Tl L$_{III}$-edge XANES spectra of (d) Tl₂O₃, P-Tl₂Ru₂O₇ and Tl₂Ru₂O₇. (e) P-Tl₂Ru₂O₇ and Tl₂Ru₂O₇ before and after ORR. (f) P-Tl₂Ru₂O₇ and Tl₂Ru₂O₇ before and after OER. (g) Schematic representations of the catalytic origin of the P-Tl₂Ru₂O₇.

activity by the mass-specific surface area, the ECSAs of Pt and Ir were obtained from the hydrogen underpotential deposition (H$_{UPD}$) method and the specific surface area of P-Tl₂Ru₂O₇ and Tl₂Ru₂O₇ were obtained from the nitrogen adsorotion-desorption measurements [36]. To obtain the electrochemical active surface area of Pt and Ir, the CV curves were recorded after reaching steady state, between 0.05 and 1.0 V vs RHE in Ar-saturated 0.1 M KOH electrolyte at a scan rate of 50 mV s⁻¹ (Figure S4). According to Eq. (4), the calculated ECSAs of Pt in 20% Pt/C and Ir in 20% Ir/C is 57.74 m² g⁻¹ and 53.94 m² g⁻¹, respectively. In addition, based on the nitrogen adsorption-desorption isotherm (Figure S5), the Brunauer-Emmett-Teller (BET) surface area of Tl₂Ru₂O₇ and P-Tl₂Ru₂O₇ is 5.2317 m² g⁻¹ and 5.2416 m² g⁻¹, respectively. Therefore, considering the obtained information of mass-specific surface area, the ORR LSV curves are normalized and showed same trend with the RDE electrode area based ORR LSV curves (Figure S6). Based on the LSV curves measured at various rotating speeds (Fig. 4(b) and S7), the Koutecky-Levich (KL) plots (Fig. 4(c) and S8) can be derived and the electron transfer number (n) as a function of applied ORR potential for P-Tl₂Ru₂O₇, Tl₂Ru₂O₇, and Pt/C can be obtained by using the slopes of

first-order linear KL plots. As shown in Fig. 4(d), P-Tl₂Ru₂O₇ exhibits the much higher n values than that of Tl₂Ru₂O₇ over the whole potential regions and these behaviors cause the higher limiting current density of P-Tl₂Ru₂O₇ than Tl₂Ru₂O₇ (Fig. 4(a)). Moreover, the P-Tl₂Ru₂O₇ represents the slightly lower n values than that of Pt/C at the potential region from 0.2 to 0.7 V (P-Tl₂Ru₂O₇ : 3.74 ~ 3.87, Pt/C : 3.83 ~ 3.91), revealing the favorable four-electron reduction of P-Tl₂Ru₂O₇.

OER LSV curves for P-Tl₂Ru₂O₇, Tl₂Ru₂O₇, Ir/C, and Pt/C catalysts are investigated by RDE technique in O₂-saturated 0.1 M KOH electrolyte and the results are shown in Fig. 5(a). The overpotentials corresponding to the current density of 10 mA cm⁻² were observed in the order of increasing values, P-Tl₂Ru₂O₇ (0.27 V) < Ir/C (0.37 V) < Tl₂Ru₂O₇ (0.45 V), representing the best OER activity of P-Tl₂Ru₂O₇. Importantly, the normalized OER LSV curves by the mass-specific surface area also show same trend with the RDE electrode area based OER LSV curves (Figure S9). Based on the OER polarization LSV curves, the smallest Tafel slope is observed for P-Tl₂Ru₂O₇ (61 mV dec⁻¹), representing the outstanding rapid oxygen evolution kinetics of
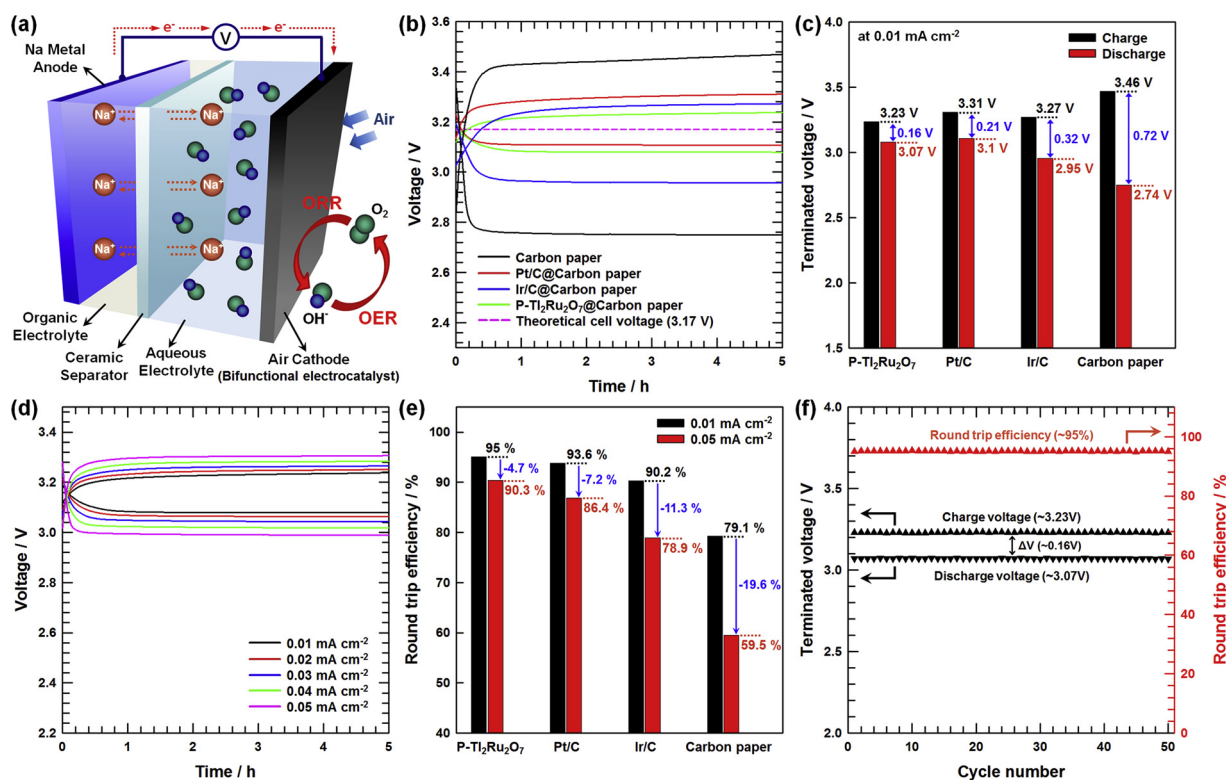
Fig. 7. (a) Schematic representations of the assembled aqueous Na-air battery. (b) Charge-discharge curves of the Na-air cell using P-Tl$_2$Ru$_2$O$_7$, Pt/C and Ir/C-coated carbon papers at a current density of 0.01 mA cm^{-2}. (c) Comparison of the overpotential gap of the carbon paper, P-Tl$_2$Ru$_2$O$_7$, Pt/C and Ir/C. (d) Charge-discharge curves of the Na-air cell using P-Tl$_2$Ru$_2$O$_7$-coated carbon papers at different current densities. (e) Comparison of the round trip efficiency of the carbon paper, P-Tl$_2$Ru$_2$O$_7$, Pt/C and Ir/C. (f) Cycling stability of P-Tl$_2$Ru$_2$O$_7$ electrode up to 50 cycles with terminated charge and discharge voltage and round trip efficiency.

dihydrogen phosphate ion functionalized Tl$_2$Ru$_2$O$_7$ (Fig. 5(b)). To further analyze the OER mechanism, the RRDE technique was employed to monitor the formation of peroxide intermediates during water oxidation (Figure S10). The disk electrode was measured at a scan rate of 10 mV s^{-1} with rotation rate of 1600 rpm, and the ring potential was fixed at 1.5 V vs RHE to oxidize the peroxide (H$_2$O$_2$) intermediates formed at the P-Tl$_2$Ru$_2$O$_7$ surface during OER. The ring current density which is significantly lower than the disk current density is detected, representing the negligible hydrogen peroxide intermediate formation and providing a favorable four-electron pathway for OER at the P-Tl$_2$Ru$_2$O$_7$ [37]. Therefore, based on the ORR and OER polarization LSV curves, the overall oxygen electrode activities are calculated by subtracting the ORR potential at a current density of -3 mA cm^{-2} from OER potential at a current density of 10 mA cm^{-2} [38]. As shown in Fig. 5(d), the smallest potential difference is observed for P-Tl$_2$Ru$_2$O$_7$ (0.67 V) compared with Pt/C (1.02 V), Ir/C (0.97 V) and Tl$_2$Ru$_2$O$_7$ (0.91 V), indicating the most outstanding oxygen electrode activity. Table S2 summarized the oxygen electrode activities for previously reported bifunctional electrocatalysts and P-Tl$_2$Ru$_2$O$_7$ shows comparable or much lower ORR and OER potential gap, representing the outstanding bifunctional catalytic activity.

### 3.3. Origin of ORR and OER catalytic activity of P-Tl$_2$Ru$_2$O$_7$ catalysts

To verify the bifunctional catalytic mechanism, we investigated the electron configurations and oxidation states of Tl and Ru ions in the Tl$_2$Ru$_2$O$_7$ and P-Tl$_2$Ru$_2$O$_7$ catalyst via *ex situ* X-ray absorption spectroscopy (XAS). Fig. 6(a) demonstrates the normalized Ru K-edge X-ray absorption near edge structure (XANES) spectra of the Ru metal, and RuO$_2$, Tl$_2$Ru$_2$O$_7$, and P-Tl$_2$Ru$_2$O$_7$ catalysts. For both Tl$_2$Ru$_2$O$_7$ and P-Tl$_2$Ru$_2$O$_7$ in Ru K-edge spectrum, there are apparent two peaks. The first peak at photon energy of 22,139 eV represents the bound of dipole-allowed transition from Ru 1 s to 5p states and the second peak

observed at 22,150 eV indicates the continuum [26,39]. After completing ORR and OER process, the Ru K-edge XANES spectra were shifted to the higher photon energies, resulting in the Ru cations are slightly oxidized (Fig. 6(b) and (c)) [40]. The Tl L$_{III}$-edge XANES spectra for Tl$_2$Ru$_2$O$_7$ and P-Tl$_2$Ru$_2$O$_7$ exhibit the major peak located at a photon energy of 12,681 eV, which is associated with the dipole-allowed transition from Tl 2p to 6d states (Fig. 6(d)) [41]. Moreover, as shown in Fig. 6(e) and (f), the positively shifted Tl L$_{III}$-edge XANES spectra are also observed, indicating that Tl cations also exhibit higher oxidation states after ORR and OER [40]. Importantly, P-Tl$_2$Ru$_2$O$_7$ shows a more positive peak shift compared to that of Tl$_2$Ru$_2$O$_7$, showing that the oxidation of Tl and Ru ions in P-Tl$_2$Ru$_2$O$_7$ occurred vigorously during the OER and ORR process, resulting in the highly efficient OER and ORR activity. These differences of oxidation degree of A and B site ions on pyrochlore oxides were explained by different surface reactivities. The reactivity of metal oxide-based materials can be determined from the environment of the metal site and the electronic structure and chemical bonding nature [42]. Therefore, the covalent character of chemical bonds can be calculated by following Eq. (8) [35]:

$$\text{Covalent character (\%)} = 100 \cdot \exp[-0.25(X_a - X_b)^2] \quad (8)$$

where X_a is the anion and X_b is the cation Pauling electronegativity values. Based on the Pauling electronegativity values of O (3.44), -OPO(OH)$_2$ (3.13), Ru (2.2), Tl (2.04), the calculated covalent character % of Ru-O and Ru-OPO(OH)$_2$ are 68.08% and 80.55% and Tl-O and Tl-OPO(OH)$_2$ are 61.26% and 74.3%, respectively. Therefore, P-Tl$_2$Ru$_2$O$_7$, which contains the Ru-OPO(OH)$_2$ and Tl-OPO(OH)$_2$ groups, possesses a higher covalent character compared with Tl$_2$Ru$_2$O$_7$. This result demonstrates that the introduced dihydrogen phosphate ion on Tl$_2$Ru$_2$O$_7$ surface can greatly improve the surface reactivity. As a result, in the 6p orbitals of Tl and 4d orbitals of Ru, the higher energy states of electrons must be existed because the high covalent character of P-Tl$_2$Ru$_2$O$_7$
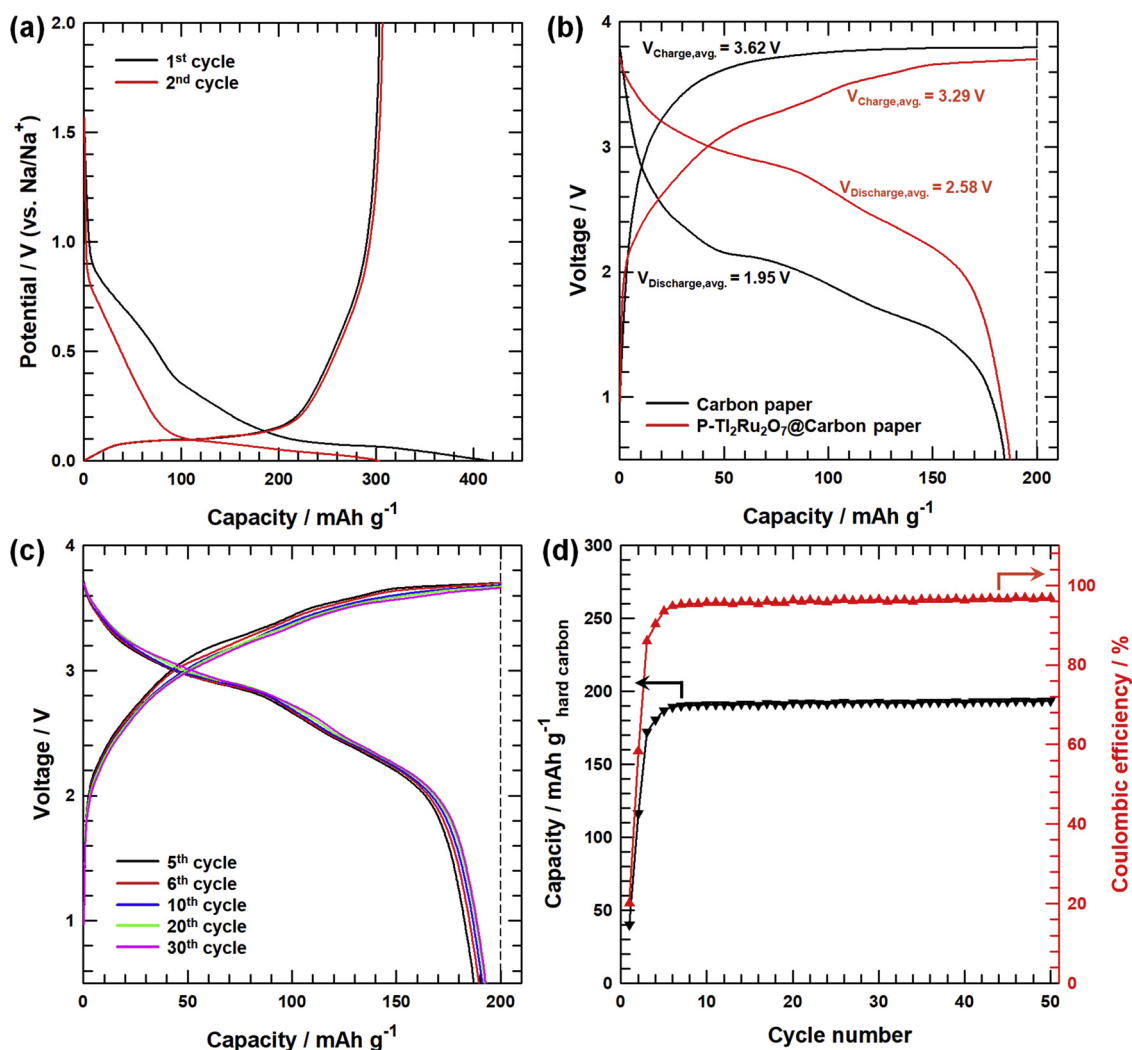
Fig. 8. (a) Galvanostatic charge-discharge voltage profiles of the half-cell with the hard carbon electrode at a current density of 20 mA g^{-1}. (b) Charge-discharge voltage profiles of the full-cells based on the bare carbon paper and P-Tl$_2$Ru$_2$O$_7$-coated carbon paper at the 5th cycle at a current density of 0.01 mA cm^{-2}. (c) Charge-discharge curves of the full cell based on the P-Tl$_2$Ru$_2$O$_7$@carbon paper for 5, 6, 10, 20 and 30th cycles at a current density of 0.01 mA cm^{-2}. (d) Cycle performance of the full cell based on the P-Tl$_2$Ru$_2$O$_7$@carbon paper at a current density of 0.01 mA cm^{-2}.

possesses a high degree of covalency. Moreover, the attraction to electrons between -OPO(OH)$_2$ and 6p and 4d orbitals of Tl and Ru cations in P-Tl$_2$Ru$_2$O$_7$ is much weaker than O element due to the low electronegativity values; thus, the electrons can be easily extracted with low energy during the oxidation of Tl and Ru ions, which results in the improved surface reactivity and fast catalyst kinetics of P-Tl$_2$Ru$_2$O$_7$.

Furthermore, the O K-edge XANES spectra of Tl$_2$Ru$_2$O$_7$ and P-Tl$_2$Ru$_2$O$_7$ represent the peak at the photon energy of 525 eV is assigned to the number of holes in the t$_{2g}$ orbital in Ru 4d and the peak located at 528 eV is associated with the number of holes in the e$_g$ orbital of Ru 4d (Figure S11) [26,43]. The P-Tl$_2$Ru$_2$O$_7$ exhibited higher absolute intensity than Tl$_2$Ru$_2$O$_7$, representing a much larger covalent Ru-O bonding characteristic in P-Tl$_2$Ru$_2$O$_7$ since the strong hybridization between Ru 4d and O 2p orbitals makes more hole density in the O 2p orbital. The degree of covalency (Figure S12) is obtained in order to quantify the covalency of Ru-O bonds of the Tl$_2$Ru$_2$O$_7$ and P-Tl$_2$Ru$_2$O$_7$ catalysts by using Eq. (9) [44]:

$$Degree \ of \ \mathrm{covalency} = \frac{\mathrm{Absorbance}}{Hole_{\,eg} + 1/4 Hole_{\,t2g}} \qquad (9)$$

The excitations of O 1 s to the Ru 4d–O 2p bands can be defined as the absorbance of Ru covalency and it can be also calculated by the integrated area between the pre-edge peak and fitted linear background

[44–46]. The quantified degree of covalency value for P-Tl$_2$Ru$_2$O$_7$ was determined to be approximately 0.75, which is a higher value than those of Tl$_2$Ru$_2$O$_7$ (0.63), metallic Pb$_2$Ru$_2$O$_{6.5}$ (0.65), and insulating Sm$_2$Ru$_2$O$_7$ (0.39) [26]. These results demonstrate that the Ru 4d and O 2p orbitals are strongly hybridized, leading to the strong Ru-O bond covalency at the surface of P-Tl$_2$Ru$_2$O$_7$ and the improved bifunctional catalytic activities. Fig. 6(g) represents the origin of the bifunctional oxygen catalytic activity for P-Tl$_2$Ru$_2$O$_7$. During the OER and ORR, the Tl and Ru ions are oxidized and the electrons are donated simultaneously. Importantly, the functionalized dihydrogen phosphate ions on the P-Tl$_2$Ru$_2$O$_7$ surface can accelerate the electron donation by promoted oxidation nature of Tl and Ru ions. Therefore, the donated electrons can easily reach to the inner layers and surface of P-Tl$_2$Ru$_2$O$_7$ and provide the low-resistance pathway during electrocatalysis due to the highly improved electron transport [40]. These results imply that we were the first to reveal the covalency effect of dihydrogen phosphate ion functionalization on the ORR and OER activities in Tl$_2$Ru$_2$O$_7$.

3.4. Na-air battery performance of P-Tl$_2$Ru$_2$O$_7$ air cathode

In order to decrease the overpotential gap and increase the round-trip efficiency for Na-air battery, the highly active bifunctional P-Tl$_2$Ru$_2$O$_7$ pyrochlore oxides was adopted as air cathode. Fig. 7(a)

displays the hybrid Na-air battery assembly, composed with ORR and OER bifunctional electrocatalyst coated air cathode in 0.1 M NaOH aqueous electrolyte, ceramic solid separator/electrolyte, and Na metal anode in 1 M $NaCF_3SO_3$/TEGDME organic electrolyte, showing the $4Na$ (s) + $2H_2O$ (l) + O_2 (g) ↔ 4NaOH (aq) of overall charge/discharge reaction [12]. Although the theoretical cell voltage of hybrid Na-air battery is 3.11 V according to the charge/discharge reaction, the fabricated Na-air battery cell voltage is calculated to be 3.17 V due to the molar concentration of NaOH solution (0.1 M) [8]. Fig. 7(b) demonstrates the charge-discharge curves for various air cathodes adopted hybrid Na-air batteries at a current density of 0.01 mA cm^{-2}. Although the deviations of plateau regions for charge and discharge curves from 3.17 V are observed for all Na-air cells, the P-$Tl_2Ru_2O_7$ air cathode adopted cell shows the smallest overpotential gap between charge and discharge plateau regions. According to the charge and discharge terminated voltages, the excellent bifunctional oxygen catalytic activity of P-$Tl_2Ru_2O_7$ air cathode results in the lowest overpotential gap with highest round trip efficiency compared with bare carbon paper, Pt/C and Ir/C at a current density of 0.01 mA cm^{-2} (Fig. 7(c)). In order to examine the rate capability, the charge-discharge curves for P-$Tl_2Ru_2O_7$ air cathode adopted cell is investigated with various the current densities, and it shows the smallest decrease in the round trip efficiency with increasing the current densities up to 0.05 mA cm^{-2} (Fig. 7(d) and (e)). In addition, the excellent cycling stability of P-$Tl_2Ru_2O_7$ air cathode adopted cell is observed by confirming the no obvious decrease of round trip efficiency during 50 cycles at a current density of 0.01 mA cm^{-2} (Fig. 7(f) and S13). Moreover, the Na-air cell with P-$Tl_2Ru_2O_7$ air cathode was found to deliver a 186.5 mW g^{-1} of maximum specific power density at a current density of 120 mA g^{-1} (Figure S14). Therefore, based on our results, P-$Tl_2Ru_2O_7$ air cathode adopted Na-air battery shows the superior electrochemical performance, especially in the cycling stability, power density and round trip efficiency, compared with other previously reported Na-air batteries (Table S3).

Finally, we fabricated Na-metal-free full cell by replacing Na metal anode to hard carbon to obtain durable cycling stability and safety. Before adopting hard carbon as anode materials, it is essential to verify the basic electrochemical performance of hard carbon by Na half coin cell. Fig. 8(a) represents the galvanostatic charge-discharge curves of hard carbon at first and second cycles and Figure S15 shows the cycling stability during 50 cycles at a current density of 20 mA g^{-1}. Because of the formation of solid electrolyte interface (SEI) layer, the large irreversible discharge capacity of hard carbon is observed at first cycle. However, after a few cycles, the coulombic efficiencies are reached to stable state with reversible charge-discharge capacity with outstanding cycling performance. Therefore, by adopting the hard carbon as anode materials instead of Na metal anode, we assembled the full cell batteries with and without the P-$Tl_2Ru_2O_7$ air cathode. The all electrochemical test of full cells were carried out with a discharging voltage cutoff of 0.5 V and charging capacity cutoff of 200 mA h g^{-1} at a current density of 0.01 mA cm^{-2}. In addition, the specific capacities of full cells were obtained by considering the loading mass of hard carbon. The charge-discharge curves of the full cell based on bare carbon paper and P-$Tl_2Ru_2O_7$ coated carbon paper at the 5th cycle were shown in Fig. 8(b). The significant decrease of voltage gap between the charge and discharge curves was observed when adopting P-$Tl_2Ru_2O_7$ air cathode by comparing the average charge-discharge voltages for full cells with and without the P-$Tl_2Ru_2O_7$ air cathode. These results were attributed to the highly improved ORR and OER catalytic activity of the P-$Tl_2Ru_2O_7$ air cathode. The discharge capacity for full cell with P-$Tl_2Ru_2O_7$ air cathode is gradually increased up to 20 cycles and saturated to be ~193 mA h g^{-1} after 20 cycles with stable cycle stability, showing high coulombic efficiencies of ~97% during 50 cycles (Fig. 8(c) and (d)). This outstanding cycling performance can be compared to bare carbon paper adopted full cell, which shows unstable cycle stability and completely loses the cycle life after 29th cycle (Figure S16).

4. Conclusions

In conclusion, we were the first to develop dihydrogen phosphate ion functionalized $Tl_2Ru_2O_7$ pyrochlore oxide nanoparticles as OER and ORR bifunctional electrocatalysts and air cathode for hybrid Na-air batteries. The outstanding bifunctional activity of P-$Tl_2Ru_2O_7$ is observed by confirming the smallest ORR and OER potential gap (0.67 V). The excellent oxygen catalytic activity of P-$Tl_2Ru_2O_7$ can be explained by the high degree of covalency of Ru-O bonds in $Tl_2Ru_2O_7$ and enhanced covalent character by dihydrogen phosphate ion functionalization, resulting in the weak attraction of electrons in Ru 4d and Tl 6p orbitals with favorable oxidation nature of Ru and Tl ions during the electrocatalysis. As a result, we successfully developed a highly enhanced round trip efficiency of aqueous Na-air battery with high power density and cycling stability by using P-$Tl_2Ru_2O_7$ as air cathode. We strongly believe that our work can suggest new insights and possibilities for effective catalytic-active pyrochlore oxides and surface modification technique for electrochemical applications.

Appendix A. Supplementary data

Supplementary material related to this article can be found, in the online version, at doi:https://doi.org/10.1016/j.apcatb.2018.12.031.

References

[1] R. Rajagopal, K.S. Ryu, Appl. Catal. B: Environ. 236 (2018) 125–139.
[2] J. Zhang, C. Zhang, Y. Zhao, I.S. Amiinu, H. Zhou, X. Liu, Y. Tang, S. Mu, Appl. Catal. B: Environ. 211 (2017) 148–156.
[3] I.S. Amiinu, X. Liu, Z. Pu, W. Li, Q. Li, J. Zhang, H. Tang, H. Zhang, S. Mu, Adv. Funct. Mater. 28 (2018) 1704638.
[4] J. Li, J. Chen, H. Wan, J. Xiao, Y. Tang, M. Liu, H. Wang, Appl. Catal. B: Environ. 242 (2019) 209–217.
[5] A. Arul, H. Pak, K.U. Moon, M. Christy, M.Y. Oh, K.S. Nahm, Appl. Catal. B: Environ. 220 (2018) 488–496.
[6] C. Li, H. Liu, Z. Yu, Appl. Catal. B: Environ. 241 (2019) 95–103.
[7] M.H. Seo, M.G. Park, D.U. Lee, X. Wang, W. Ahn, S.H. Noh, S.M. Choi, Z.P. Cano, B. Han, Z. Chen, Appl. Catal. B: Environ. 239 (2018) 677–687.
[8] S.H. Sahgong, S.T. Senthilkumar, K. Kim, S.M. Hwang, Y. Kim, Electrochem. Commun. 61 (2015) 53–56.
[9] Z. Khan, B. Senthilkumar, S. Park, S. Park, J. Yang, J. Lee, H. Song, Y. Kim, S. Kwak, H. ko, J. Mater. Chem. A 5 (2017) 2037–2044.
[10] Y. Wu, X. Qiu, F. Liang, Q. Zhang, A. Koo, Y. Dai, Y. Lei, X. Sun, Appl. Catal. B: Environ. 241 (2019) 407–414.
[11] B. Senthilkumar, Z. Khan, S. Park, I. Seo, H. Ko, Y. Kim, J. Power Sour. 311 (2016) 29–34.
[12] J. Cheon, K. Kim, Y. Sa, S. Sahgong, Y. Hong, J. Woo, S. Yim, H. Jeong, Y. Kim, S. Joo, Adv. Energy Mater. 6 (2016) 1501794.
[13] Y. Hu, X. Han, Q. Zhao, J. Du, F. Cheng, J. Chen, J. Mater.Chem. A 3 (2015) 3320–3324.
[14] Z. Khan, S. Park, S.M. Hwang, J. Yang, Y. Lee, H.-K. Song, Y. Kim, H. Ko, NPG Asia Mater. 8 (2016) e294.
[15] Q. Sun, H. Yadegari, M.N. Banis, J. Liu, B. Xiao, B. Wang, S. Lawes, X. Li, R. Li, X. Sun, Nano Energy 12 (2015) 698–708.
[16] Y. Li, H. Yadegari, X. Li, M.N. Banis, R. Li, X. Sun, Chem. Commun. 49 (2013) 11731–11733.
[17] W. Wan, X. Liu, H. Li, X. Peng, D. Xi, J. Luo, Appl. Catal. B: Environ. 240 (2019) 193–200.
[18] Y.Q. Zhang, M. Li, B. Hua, Y. Wang, Y.F. Sun, J.L. Luo, Appl. Catal. B: Environ. 236 (2018) 413–419.
[19] G. Zhang, S. Wollner, Appl. Catal. B: Environ. 222 (2018) 26–34.
[20] A. Sivanantham, P. Ganesan, S. Shanmugam, Appl. Catal. B: Environ. 237 (2018) 1148–1159.
[21] M. Sakthivel, J. Drillet, Appl. Catal. B: Environ. 231 (2018) 62–72.
[22] W. Li, Y. Xiong, Z. Wang, M. Bao, J. Liu, D. He, S. Mu, Appl. Catal. B: Environ. 231 (2018) 277–282.
[23] A. Zubiaur, N. Job, Appl. Catal. B: Environ. 225 (2018) 364–378.
[24] P. Tan, B. Chen, H. Xu, W. Cai, W. He, M. Ni, Appl. Catal. B: Environ. 241 (2019) 104–112.
[25] H. Wang, F.X. Yin, B.H. Chen, X.B. He, P.L. Lv, C.Y. Ye, D.J. Liu, Appl. Catal. B: Environ. 205 (2017) 55–67.
[26] J. Park, M. Risch, G. Nam, M. Park, T. Shin, Park S, M. Kim, Y. Horn, J. Cho, Energy

Environ. Sci. 10 (2017) 129–136.
[27] K. Fujii, Y. Sato, S. Takase, Y. Shimizu, J. Electrochem. Soc. 162 (2015) 129–135.
[28] J. Parrondo, M. George, C. Capuano, K.E. Ayers, V. Ramani, J. Mater. Chem. A 3 (2015) 10819–10828.
[29] J.B. Goodenough, R. Manoharan, M. Paranthaman, J. Am. Chem. Soc. 112 (1990) 2076–2082.
[30] H.S. Horowitz, J.M. Longo, H.H. Horowitz, J. Electrochem. Soc. 130 (1983) 1851–1859.
[31] Y.-U. Kwon, E.-O. Chi, S.-I. Mho, Bull. Korean Chem. Soc. 18 (1997) 972–976.
[32] K.T. Lee, B.W. Lee, M.A. Camaratta, E.D. Wachsman, RSC Adv. 3 (2013) 19866–19871.
[33] J. Prakash, D.A. Tryk, E.B. Yeager, J. Electrochem. Soc. 146 (1999) 4145–4151.
[34] W. Jo, J. Jang, K. Kong, H. Kang, J. Kim, H. Jun, K. Parmar, J. Lee, Angew. Chem. Int. Ed. 51 (2012) 3147–3151.
[35] T. Zhai, L. Wan, S. Sun, Q. Chen, J. Sun, Q. Xia, H. Xia, Adv. Mater. 29 (2017) 1604167.
[36] B. Qin, H. Yu, J. Chi, J. Jia, X. Gao, D. Yao, B. Yi, Z. Shao, RSC Adv. 7 (2017) 31574–31581.
[37] K. Rui, G. Zhao, Y. Chen, Y. Lin, Q. Zhou, J. Chen, J. Zhu, W. Sun, W. Huang, S.X. Dou, Adv. Funct. Mater. 28 (2018) 1801554.
[38] G. Fu, Z. Cui, Y. Chen, Y. Li, Y. Tang, J. Goodenough, Adv. Energy Mater. 7 (2017) 1601172.
[39] J.-H. Choy, S.-H. Hwang, G. Demazeau, D.-Y. Jung, J. Le, J. Phys. IV 7 (1997) C2-763–C2-764.
[40] J. Park, M. Park, G. Nam, M. Kim, J. Cho, Nano Lett. 17 (2017) 3974–3981.
[41] G.H. Kwei, C.H. Booth, F. Bridges, M.A. Subramanian, Phys. Rev. B 55 (1997) 688–692.
[42] C. Liu, C. Zhang, H. Fu, X. Nan, G. Cao, Adv. Energy Mater. 6 (2016) 1601127.
[43] A. Braun, S. Erat, A.K. Ariffin, R. Manzke, H. Wadati, T. Graule, L.J. Gauckler, Appl. Phys. Lett. 99 (2011) 202112.
[44] J. Suntivich, W.T. Hong, Y. Lee, J.M. Rondinelli, W. Yang, J.B. Goodenough, B. Dabrowski, J.W. Freeland, Y.S. Horn, J. Phys. Chem. C 118 (2014) 1856–1863.
[45] J. Suntivich, H.A. Gasteiger, N. Yabuuchi, H. Nakanishi, J.B. Goodenough, Y. Shao-Horn, Nat. Chem. 3 (2011) 546–550.
[46] J. Suntivich, K.J. May, H.A. Gasteiger, J.B. Goodenough, Y. Shao-Horn, Science 334 (2011) 1383–1385.